THE JOURNAL OF PHYSICAL CHEMISTRY C
A JOURNAL OF THE AMERICAN CHEMICAL SOCIETY

pubs.acs.org/JPCC
Article

Quantitative Chemical Mapping of Pt/Rh Gauze Catalysts for Ammonia Oxidation using Resonant X-ray Tomography

Srashtasrita Das, Michael E. Stuckelberger, Jan Pottbacker, Sven Jakobtorweihen, Christian G. Schroer, Raimund Horn, and Thomas L. Sheppard*

Cite This: J. Phys. Chem. C 2024, 128, 5053−5063
Read Online

ABSTRACT: The loss of platinum group metals during the industrial Ostwald process for catalytic ammonia oxidation is a century-old concern. Understanding catalyst degradation requires knowledge of physicochemical changes occurring on stream, particularly on technical Pt/Rh gauze catalysts. However, such catalysts are mainly studied with surface-sensitive methods or as model systems since their composition of noble metals (e.g., 95/5 wt % Pt/Rh) makes it challenging to characterize the bulk catalyst. Here, we exploit the high-resolution and elemental sensitivity of synchrotron-based hard X-ray resonant tomography to quantify the 3D distribution of Rh and Pt in technical gauze catalysts. Resonant tomography performed above and below the Rh K-edge (23.300 and 23.208 keV, respectively) allowed computation of elemental distribution. Absorption contrast tomography was successful despite beam transmission of <0.1%. This was achieved using a single-photon counting detector. Rh segregation, Pt loss, and bulk material degradation leading to redistribution of elements were visualized and quantified within intact ∼76 μm diameter wires, with 2 μm resolution, and up to 50 days on stream. The estimated local Pt and Rh wt % changes showed significant material loss from the wire exterior and characteristic protrusions. However, the wire core was unaffected by the reaction conditions even after 50 days on stream. No volume diffusion from the wire center to the exterior was observed to mitigate material loss from the latter. This flexible and high-throughput quantitative imaging approach is uniquely possible with synchrotron hard X-ray tomography, opening further routes of study for compositionally challenging industrial catalysts.

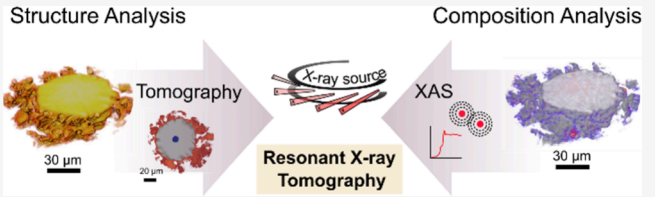

1. INTRODUCTION

Catalytic oxidation of ammonia (NH_3) to nitric oxide (NO), the first step in the Ostwald process for industrial nitric acid (HNO_3) production, uses woven or knitted Pt-alloy gauzes due to their excellent yield and selectivity to NO.[1,2] This reaction is among the most important in industrial chemistry as a key step in manufacturing nitrate-based fertilizers.[2] Industrial NH_3 oxidation involves high temperatures (800−950 °C) and elevated pressures of corrosive gas feed (5−12 bar).[1,2] Under these harsh conditions, the smooth surfaces of the fresh catalyst gauze wires undergo severe degradation in the form of cauliflower-like protrusions.[3,4] Initially, the increased catalyst surface area improves the catalytic activity and space-time yield of NO.[5,6] Progressive degradation later increases the formation of undesired nitrous oxide as a byproduct.[2] Subsequent loss of platinum group metals (PGMs) from the gauzes has been shown to account for roughly 27% catalyst loss after 120 days of industrial operation at medium pressures.[7] Material loss, mainly as volatile oxides (e.g., $PtO_{2(g)}$), eventually leads to mechanical failure of the catalyst.[1,5] Similar catalyst degradation is also encountered for other processes using gauze-type catalysts, including HCN synthesis.[8,9] Given that global HNO_3 production amounted to ∼70 million tons (USD 24 billion) in 2020,[10] PGM loss increases process costs and can result in wastage of finite resources unless carefully controlled.[11] Early efforts to prevent or mitigate PGM loss led to the use of alloys such as Pt/Rh, since Rh (e.g., > 2 wt %) strengthens the mechanical integrity of the gauze.[2,4] However, Rh is also an active catalyst under industrial NH_3 oxidation conditions and is known to increase selectivity to N_2 as a byproduct.[12] An alternate strategy to mitigate PGM loss involves placing Pd-based catchment gauzes to trap volatile $PtO_{2(g)}$ species downstream. However, these gauzes can also suffer degradation and cause additional PGM wastage.[7,13,14]

Despite considerable research, the inability to eliminate PGM loss persists even after a century of industrial operation. This highlights the potential for improvement in catalyst design and stimulates the need to study structural and chemical factors affecting gauze degradation. However, it is quite challenging to characterize technical catalysts made entirely of bulk noble metal in a representative manner. Scanning

Received: January 3, 2024
Revised: February 22, 2024
Accepted: February 26, 2024
Published: March 18, 2024

https://doi.org/10.1021/acs.jpcc.4c00041
J. Phys. Chem. C 2024, 128, 5053−5063

electron microscopy (SEM) has revealed surface deformations such as step edges with different facets and etch pits resulting from hotspots formed during wire degradation, showing progressive protrusion growth under reaction conditions.[4,15] Chemical speciation studies by X-ray photoelectron spectroscopy (XPS) and energy-dispersive spectroscopy on industrial gauzes showed higher Rh enrichment at the grain boundaries and increasing Rh/Pt ratio as a function of operating pressures.[7] Atom probe tomography (APT) has been used to monitor the segregation of PGM species and local gauze composition revealing the formation of metal oxides in 3D space with near-atomic scale spatial resolution.[16,17] However, such characterization is either limited to the outermost surface (i.e., SEM, XPS) or is possible only on nm-sized subvolumes (APT). The use of surface-sensitive or highly localized techniques risks the acquisition of unrepresentative data, given the heterogeneous structure and characteristic length scale of the gauze wires in the parent catalyst (e.g., 60−80 μm). Furthermore, the inability to reproduce the harsh reaction conditions for *in situ* or *operando* experiments has necessitated model catalyst studies, such as ideal surfaces or supported PGM nanoparticles.[18−20] Early attempts to study the local variation of Rh content using electron microprobe analysis (EMP) allowed semiquantitative analysis of wire cross sections and individual protrusions. Subsequent qualitative X-ray diffraction (XRD) analysis showed Rh enrichment around the hollow structures of these specimens.[4] However, this was only possible after cutting and polishing, which is both time-consuming and clearly carries risks of invasive sample preparation.

As an alternative, hard X-ray tomography (X-ray CT) can offer noninvasive 3D imaging of physical and chemical structures in complex solids, including technical or industrial catalysts.[21,22] Laboratory X-ray CT has previously visualized degradation and bulk PGM loss in Pt/Rh gauzes in terms of surface geometry, but without any information regarding chemical composition.[23] Recently, the surface degradation of Pd-based catchment gauzes was visualized using *in situ* synchrotron X-ray CT in absorption-contrast under model aging conditions in air. Quantitative composition changes could not be retrieved in these gauzes due to the phase-contrast artifacts resulting in an artificial intensity profile within the wire.[13] Despite the excellent potential of hard X-ray tomography for quantitative 3D analysis of large samples, it has to the best of our knowledge never been successfully used to obtain quantitative local chemical composition of Pt/Rh gauzes. This can be attributed to the pure PGM content of Pt/Rh gauze catalysts, which are woven or knitted out of ∼76 μm diameter wires. Such samples are challenging to study in their native form without invasive subsampling due to extreme X-ray beam attenuation. X-ray fluorescence tomography for example can acquire 3D spatial chemical information, but with large samples, this imposes the phenomenon of X-ray self-absorption and attenuation, which hinders quantitative evaluation.[24] Furthermore, using tomographic X-ray absorption spectroscopy to yield structural/chemical information across an entire absorption edge is time-consuming and likewise suffers from extreme X-ray beam attenuation.[25,26] Combining X-ray absorption spectroscopy with scanning transmission X-ray tomography (STXM-CT) at only two energies, above and below an absorption edge, can in principle recover the local chemical composition of industrial catalysts at μm to the nm scale, while probing morphological changes.[27] This concept was previously demonstrated on catalysts used for fluid catalytic cracking, for example, by Weckhuysen and Meirer et al.[28,29] However, the use of conventional area-detectors such as CCD/CMOS is entirely unsuitable for 76 μm diameter wires of pure noble metal due to extremely low transmission at the energy of the Rh K-edge. On the other hand, the high dynamic range of a single-photon counting pixel detector offers the feasibility of a lossless measurement technique for characterization of these PGM catalysts and other highly absorbing samples.[30]

In this study, we implement a spatially resolved approach to tackle the challenge of studying industrial Pt/Rh gauze catalysts consisting purely of noble metals (∼76 μm diameter wires). STXM-CT recorded using a single-photon counting detector enabled visualization and quantification of the local elemental distribution of Pt and Rh via the Beer−Lambert law. By performing resonant STXM-CT above and below the Rh K-edge (Figure 1), regions of Pt loss and Rh segregation were

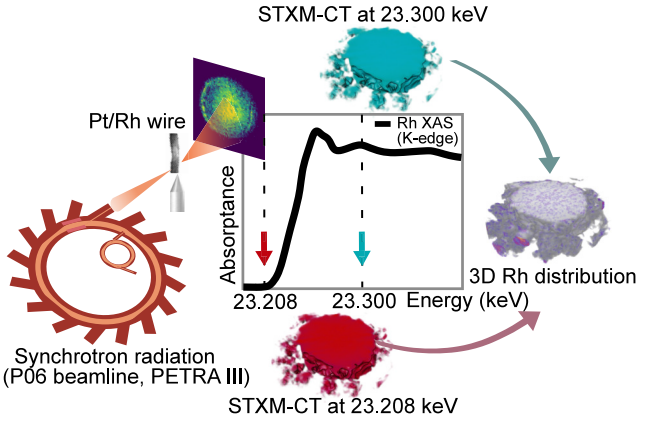

Figure 1. Illustration of the hard X-ray resonant STXM-CT around the Rh K-edge for studying elemental composition changes of a single Pt/Rh gauze wire using synchrotron radiation, thereby revealing the local 3D distribution of each element within the catalyst.

observed locally (∼2 μm resolution) for typical Pt/Rh gauze catalysts aged under industrial NH_3 oxidation conditions for 24 to 100 h in a bench-scale reactor[31] and up to 50 days in a pilot plant. This quantitative study of local compositional changes can specify the extent of Pt loss and Rh segregation leading to a redistribution of metals with advanced aging. By measuring entire wires, this constitutes a high-throughput study while avoiding invasive sample preparation common to comparable analyses such as EMP or focused ion beam (FIB) sectioning. The data presented here, at the acquisition rate and sample size demonstrated, is only accessible with synchrotron radiation-based STXM-CT and accomplishes a longstanding goal in industrial chemistry to quantify the chemical degradation of PGM gauze catalysts at technical rather than model scale.

2. METHODS

2.1. Sample Preparation. Fresh Pt/Rh gauzes (∼76 μm wire diameter, 5 wt % Rh) were provided by Yara International ASA (Oslo, Norway). Aging was performed under typical industrial NH_3 oxidation conditions in a bench-scale reactor at TUHH at an absolute pressure of 5 bar, inlet temperature of 300 °C, and feed composition of $NH_3/O_2/Ar/N_2$ = 10/18.6/2/69.4 mol %.[31] Gauzes were removed from the reactor after 24, 50, and 100 h aging time. The first gauze (toward the inlet)

https://doi.org/10.1021/acs.jpcc.4c00041
J. Phys. Chem. C 2024, 128, 5053−5063

from a treated stack of 10 gauzes was chosen due to an expected higher degree of degradation from exposure to a maximum concentration of NH_3 and O_2.[2,4] To investigate the extent of catalyst degradation after an extended industrial operation, another gauze was provided by Yara International ASA following 50 days of operation in an NH_3 oxidation pilot plant. The extent of degradation was first studied for all catalysts using SEM.[32] Single wires were carefully extracted from all aged Pt/Rh gauzes using a scalpel and tweezers. Individual wires (typical length 5 mm) were mounted using superglue on aluminum tomography pins for further STXM-CT studies.

2.2. Resonant STXM-CT Data Acquisition. X-ray resonant STXM-CT experiments were performed at the hard X-ray microprobe beamline P06 of PETRA III at the Deutsches Elektronen-Synchrotron DESY (Hamburg, Germany). The beam was focused to a spot size of 200 × 200 nm^2 at 23.300 keV using a stack of 149 Be compound refractive lenses.[33] The sample was placed out of the beam focus for scan time optimization, resulting in a beam spot size of 1.2 × 1.5 μm^2 (horizontal × vertical). A suitable sample region of interest was chosen and aligned within the center of rotation with respect to the X-ray beam using a PCO edge camera (Excelitas PCO GmbH, Kelheim, Germany). The transmitted beam intensities were recorded using an in-vacuum EIGER X 4M pixel detector (DECTRIS AG, Baden, Switzerland) having a detector pixel size of 75 μm and a frame size of 2070 × 2167 pixels. The detector was positioned downstream at the nanoprobe endstation of the P06 beamline at 8.5 m from the sample. STXM-CT data was recorded in scanning with absorption-contrast mode. 2D projections were obtained using bidirectional fly scans in a raster pattern with an acquisition step size of 0.5 μm in both horizontal y-direction (on-the-fly or fast-motor axis) and vertical z-direction (step or slow-motor axis) and an exposure time of 2 ms. The signal within a defined region of interest in the detector at each scan point was summed over the detector panels to generate each pixel value. This combined map generated from the pixel values at each y- and z-position was used to generate a single projection at each rotation angle. This resulted in an acquisition time of <2 min for each projection. The rotational axis was used as the third (slow) axis for the STXM-CT tomographic data sets, which were acquired as a series of 4 subtomograms. Each subtomogram had an angular step size of 8° between the consecutive projections. There was a 2° offset between each subtomogram. These subtomograms helped ensure 360° acquisition of a tomographic data set, so that the data acquisition is not hindered in case of any experimental issues. A total of 184 projections were therefore acquired for each STXM-CT measurement, resulting in an acquisition time of 5 h for each complete tomogram. It should be noted that this measurement technique was not optimized for speed and has a significant scope for improvement in future measurements. Individual steps for projection generation and tomographic reconstruction are described in SI section 2.1. Two STXM-CT scans were carried out at each measurement position for each sample, one scan above (23.300 keV) and one scan below (23.208 keV) the Rh K-edge of 23.220 keV.

2.3. STXM-CT Data Processing. Each recorded projection was generated using in-house scripts in Python,[34−36] with steps detailed in SI section 2. All 3D tomographic reconstructions for the wire volumes from the STXM-CT projection series were carried out using the simultaneous iterative reconstruction technique (SIRT),[37] via the ASTRA Toolbox and Python.[38,39] Comparison between measured transmitted X-ray intensity and expected theoretical transmission was done to validate the feasibility of tomographic reconstructions. Quantitative STXM-CT reconstructions were verified using a tomography consistency check (SI section 2.3). The STXM-CT volumes were rendered and segmented using Avizo software (Thermo Fisher Scientific) and Fiji (a distribution of ImageJ).[40,41] The tomogram sets recorded above and below the Rh K-edge were aligned for quantitative elemental composition study. Detailed data analysis involving quantitative assessment of morphological and composition changes (SI section 3−5) was conducted using Python.

2.4. Density Estimation Using the Beer−Lambert Law. The calculation of the volumetric material density for Pt and Rh relies on the Beer−Lambert law. In its generalized form, the Beer−Lambert law readsfor an X-ray beam with

$$I = I_0 \cdot \exp\left\{-\sum_{i=0}^{N} \underbrace{\sum_{j=0}^{M_j} \left(\frac{\mu}{\rho}\right)_j \cdot \rho_{ij}}_{\mu_i} \cdot x_i\right\} = I_0 \cdot \exp\left\{-\sum_{i=0}^{N} \mu_i \cdot x_i\right\} \quad (1)$$

incident intensity I_0 that passes N voxels with indices i, each filled with M_j elements with mass density ρ_{ij}. The mass attenuation coefficient $\left(\frac{\mu}{\rho}\right)_j$ is a material constant tabulated for each chemical element and X-ray energy in the literature.[42] Its multiplication with ρ_{ij} and subsequent summation over all elements in the specific voxel yield the linear absorption coefficient μ_i. Finally, x_i is the path length of the X-ray in voxel i and I is the transmitted X-ray intensity.

The tomographic reconstruction algorithm (see SI section 2.1) yields the experimentally determined μ_i for each voxel and for both tomograms measured at the energies E' = 23.208 keV and E'' = 23.300 keV. For the Pt/Rh material system, this yields a set of 2 linear equations with 2 variables:

$$\mu_i^{E'} = \left(\frac{\mu}{\rho}\right)_{\mathrm{Pt}}^{E'} \cdot \rho_{i,\mathrm{Pt}} + \left(\frac{\mu}{\rho}\right)_{\mathrm{Rh}}^{E'} \cdot \rho_{i,\mathrm{Rh}} \quad (2)$$

$$\mu_i^{E''} = \left(\frac{\mu}{\rho}\right)_{\mathrm{Pt}}^{E''} \cdot \rho_{i,\mathrm{Pt}} + \left(\frac{\mu}{\rho}\right)_{\mathrm{Rh}}^{E''} \cdot \rho_{i,\mathrm{Rh}} \quad (3)$$

With $\mu_i^{E'}$ and $\mu_i^{E''}$ measured, and $\left(\frac{\mu}{\rho}\right)_{\mathrm{Pt}}^{E'}$ = 51.38 $cm^2\ g^{-1}$, $\left(\frac{\mu}{\rho}\right)_{\mathrm{Pt}}^{E''}$ =50.86 $cm^2\ g^{-1}$, $\left(\frac{\mu}{\rho}\right)_{\mathrm{Rh}}^{E'}$ = 10.8 $cm^2\ g^{-1}$, and $\left(\frac{\mu}{\rho}\right)_{\mathrm{Rh}}^{E''}$ =63.8 $cm^2\ g^{-1}$, known from the literature, this system was solved for every voxel, yielding $\rho_{i,\mathrm{Pt}}(x, y, z)$ and $\rho_{i,\mathrm{Rh}}(x, y, z)$ as two 3D density matrices for Pt and Rh, respectively.

3. RESULTS AND DISCUSSION

3.1. Geometry of the Pt/Rh Catalyst Series with Time on Stream. Resonant STXM-CT measurements were performed on identical sample volumes of each wire. Reconstructed volumes of single wires at either energy were sufficient to reveal catalyst degradation in the form of characteristic protrusions (Figure 2). SEM images showing surface deformations of each catalyst are included for comparison, confirming degradation within 24 h (Figure 2 and SI section 1). The tomograms have a 3D sampling region (voxel) size of 0.5 × 0.5 × 0.5 μm^3 and an estimated spatial

https://doi.org/10.1021/acs.jpcc.4c00041
J. Phys. Chem. C 2024, 128, 5053−5063

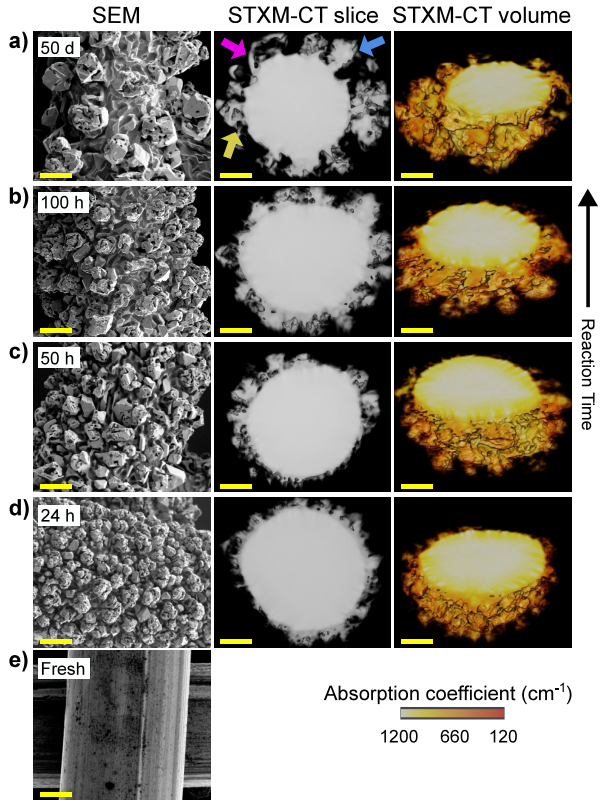

Figure 2. Increasing degradation of Pt/Rh wires during NH_3 oxidation, studied as a function of time on stream after: (a) 50 days, (b) 100 h, (c) 50 h, (d) 24 h. Colored arrows indicate specific features of interest. Deformations are visualized on the external surface by SEM (left column), orthographic projection of STXM-CT data (middle column), and reconstructed 3D volumes (right column). The color bar represents the measured absorption coefficient (μ) per voxel of the reconstructed 3D volume. The smooth surface of a fresh Pt/Rh gauze is shown in panel (e). Scale bars are 20 μm.

resolution of ~2.2 μm (SI section 2.2), with degradation clearly visible at this resolution even after 24 h on stream.

STXM-CT allowed for detailed visualization of catalyst degradation in terms of measured absorption coefficient (μ) (Figure 2). Diverse structures were observed including individual porous protrusions (blue arrow), highly corroded protrusions with severe material loss (yellow arrow), and completely hollow structures similar in appearance to bubbles (pink arrow). Statistical evaluation of the protrusion sizes formed around the wire was performed over a large vertical field of view (29 μm), showing progressive protrusion growth with time on stream (SI section 3.3).[4] The calculated average protrusion size supports literature SEM measurements, validating the observed aging behavior characteristic of industrial Pt/Rh gauzes.[4,43]

Different PGM loss mechanisms have been proposed in the literature, including surface diffusion and volume diffusion.[3,4] While surface erosion of Pt/Rh gauzes is well-known, the volume diffusion of metals, if any, could in principle also affect interior regions closer to the wire center. Here, the dimensions of the wire interior were estimated using horizontal Feret diameters. No significant changes were observed from 24 to 100 h (Table 1 and SI section 3.1). This suggests that the inner wire remained unaffected during the formation of surface protrusions despite extensive material loss from the wire exterior. The clearly diminished wire diameter after 50 days of operation shows substantial and progressive material loss with time on stream. However, and as observed in previous literature studies,[13,23] it is not possible to state purely from shape analysis alone whether only surface diffusion or also volume diffusion plays a role. This was later analyzed with resonant STXM-CT by quantifying the local Pt and Rh composition.

Table 1. Structural Changes of Pt/Rh Wires with Aging Time Compared to a Fresh Wire

time on stream	mean Feret diameter of wire interior (μm)[a]	protrusion size (μm)[b]	surface area (μm^2)[c]	surface area factor[e]
0 h	76[d]	n.a.	6900	1.0
24 h	73.3 ± 2.5	10.8 ± 2.6	28061	4.1
50 h	73.9 ± 2.5	14.3 ± 3.5	28461	4.1
100 h	72.2 ± 4.0	16.6 ± 3.8	40698	5.9
50 d	64.5 ± 1.5	21.2 ± 5.2	34432	5.0

[a]Measured at 18 equidistant positions per slice of the entire sample volume. [b]Measured on radial axis, approximated to circular diameter (SI Table S6). [c]Surface area calculated for 58 slices per sample, equivalent to 29 μm wire height, and represent a lower limit as porosity below the spatial resolution of tomograms is not considered. [d]Measured by SEM to confirm the fresh wire dimension. [e]Calculated as surface area of aged gauze divided by the surface area of the fresh gauze.

The effect of degradation on the catalyst surface area was studied for a cropped volume of 29 μm, showing an increased surface area of the aged gauzes by a factor of 4−6 compared to the fresh gauze (Table 1 and SI section 3.2). The latter was calculated from computational fluid dynamics modeling in previous work.[31] However, the subsequent decrease in surface area after 50 days on stream can be attributed to the widespread breakage of protrusions from the surface. This can also be observed by the rugged texture of the wire surface, with only a few large protrusions present (Figure 2a).

It should be noted that accurate geometric parameters such as protrusion size and wire surface area are best obtained by X-ray CT, which provides 3D spatially resolved data. SEM can provide only surface analysis, unless cross sections are prepared. Obtaining comparable morphological information by FIB slice tomography for 29 μm-tall wire sections would be prohibitively time-consuming. Furthermore, FIB slice tomography is invasive/destructive and has well-known artifacts during study of porous media in the absence of a contrast or filling agent.[44] However, the results in Table 1 are only representative of gauze subsections. They may not be sensitive to wire inhomogeneities,[6] observed at intersections and in proximity to the reactor wall (SI Figures S1−S5). TEM studies provide depth information for thin samples, revealing morphological changes in the range of hundreds of nm, which is typically not representative of the entire sample. In the case of pure PGM catalysts, this might not be possible due to extreme beam attenuation. Techniques such as nitrogen sorption and mercury porosimetry, which are commonly used to measure surface area and pore volumes in catalysis, provide bulk-averaged information, and do not provide spatial information with depth-profiling, which can be achieved using X-ray CT.[45] Hence, measuring large volumes by X-ray CT provides a more accurate portrayal of the heterogeneity in technical catalysts than contemporary imaging methods. Notably, the results shown above are a routine application of X-ray CT and reveal no chemical information on the local

https://doi.org/10.1021/acs.jpcc.4c00041
J. Phys. Chem. C 2024, 128, 5053−5063

sample composition. For this purpose, the effects of catalyst degradation in terms of material density were further explored below, with local Pt and Rh concentrations examined by resonant STXM-CT.

3.2. Quantification of Pt/Rh Loss with Time on Stream. The individual absorption coefficient values from each voxel obtained from STXM-CT can be used to interpret changes in material properties. Interpreting μ based on single-energy tomograms is ambiguous, as both local elemental composition and mass density can impact μ. However, changes in shape accompanied by a decrease in μ strongly suggest material loss. To visualize this effect, radial segments were plotted along with resulting segment histograms (Figure 3a,b). Based on this approach, regions of interest (ROIs) were then identified for tomograms of a fixed height (29 μm), which were segmented according to the extreme interior ("core"), the extreme exterior ("cauliflower"), and the intermediate region between ("donut") (Figure 4a and SI section 2.4). The results confirm a strong decrease in μ from the core ROI to the cauliflower ROI (Figure 3c). This corresponds to an average μ in the protrusions (<400 cm^{-1}) much less than 30% that of the core (1000−1200 cm^{-1}), illustrating significant material loss along with characteristic degradation with protrusion formation (Figure 2). While degradation of Pt/Rh gauzes in the form of exterior protrusions indicates surface degradation,[4] the progressive change in μ around the outer donut ROI and the cauliflower ROI shows that the observed material loss process may be more complex, as discussed later during the quantitative analysis. This again points to the value of spatially resolved tomography over surface analysis in analyzing such heterogeneous samples.

The extent of material loss in each catalyst wire was further evaluated by inspecting histogram values of μ for each ROI (Figure 4). The μ of the core ROI followed a normal distribution and was constant with increasing time on stream, indicating uniform composition even after 50 days, and therefore the absence of any bulk or volume diffusion affecting the core. The cauliflower ROI showed a right-skewed distribution with comparatively low μ values (maxima at ~40 cm^{-1}) in agreement with the expected loss of Pt from the wires. The increase in histogram counts for the cauliflower ROI from 24 to 100 h indicates progressive protrusion growth resulting in a higher voxel count within this ROI. Similarly, lower counts after 50 days result from characteristic breakage of individual protrusions, as shown by SEM and STXM-CT (Figure 2). The increase in protrusion size from 24 h to 50 days also appears to correlate with increased material loss from the outer regions of the donut ROI. The development of a bimodal histogram after 24 h shows the different extent of material loss within the donut ROI and hence the wire inhomogeneity. However, after 100 h of reaction time, the bimodal peak converges into a unimodal peak after 50 days on stream, indicating extreme material loss eventually affecting the donut ROI. This is consistent with the observed decrease in the Feret diameter of the wire interior (Table 1).

3.3. Quantification of Local Pt and Rh Distribution by Resonant STXM-CT. As shown above, studying the morphological changes within the Pt/Rh wires was possible with X-ray CT even at a single energy, providing information about the extent of wire degradation and protrusion growth with time on stream. To expand on this, we acquired STXM-CT data sets of identical regions at two energies around the Rh K-edge (23.208 and 23.300 keV). This provides sensitivity to

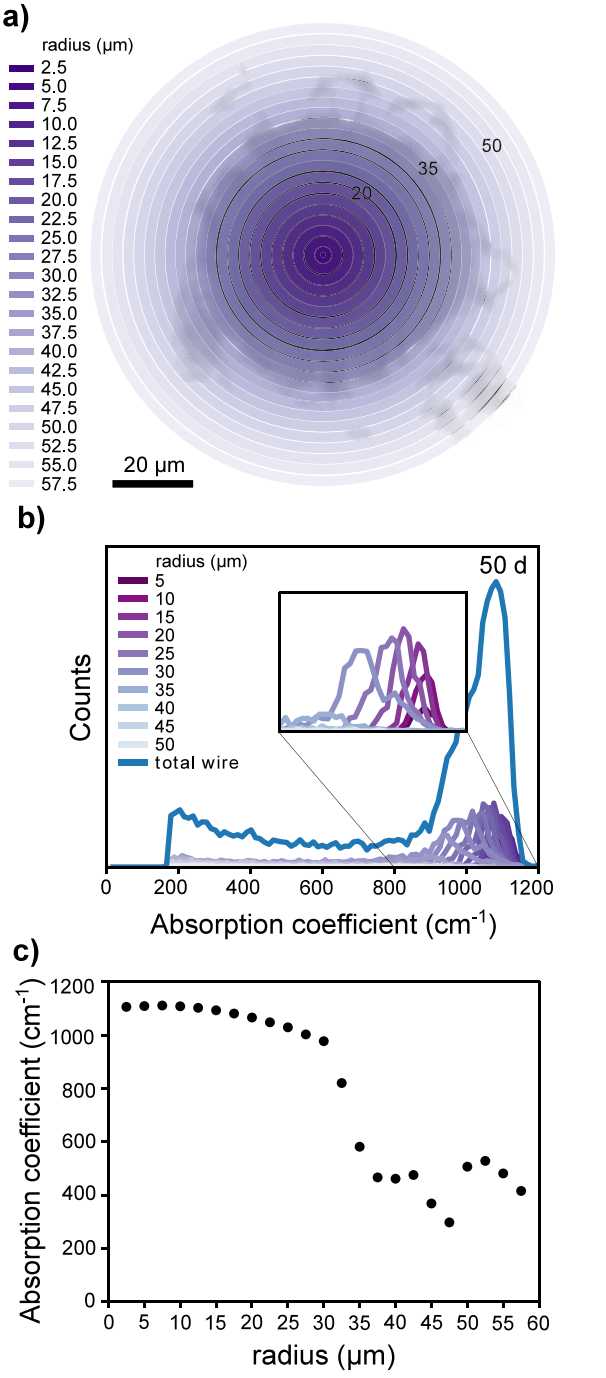

Figure 3. Wire inhomogeneity due to aging was visualized using (a) concentric radial segments with increasing radius (r) of 2.5 μm from the center point (shown on a 50 days aged sample at 23.300 keV) and (b) corresponding histogram of each radial segment. The inset in panel (b) highlights μ values from the wire core. (c) Average μ of radial segments as a function of r, quantifying wire inhomogeneity and indicating material loss.

Rh content within the sample, as indicated by the shift in histogram values of the core and donut ROIs (Figure 4). The local Pt and Rh densities can therefore be quantified based on the known initial composition of 95/5 wt % Pt/Rh, sequential measurements around the Rh K-edge, and the corresponding change in μ for Pt (with μ for ambient air being negligible) at the selected energy points (section 2.4, eqs 2 and 3). While previous attempts showed qualitative or bulk averaged Rh

https://doi.org/10.1021/acs.jpcc.4c00041
J. Phys. Chem. C 2024, 128, 5053−5063

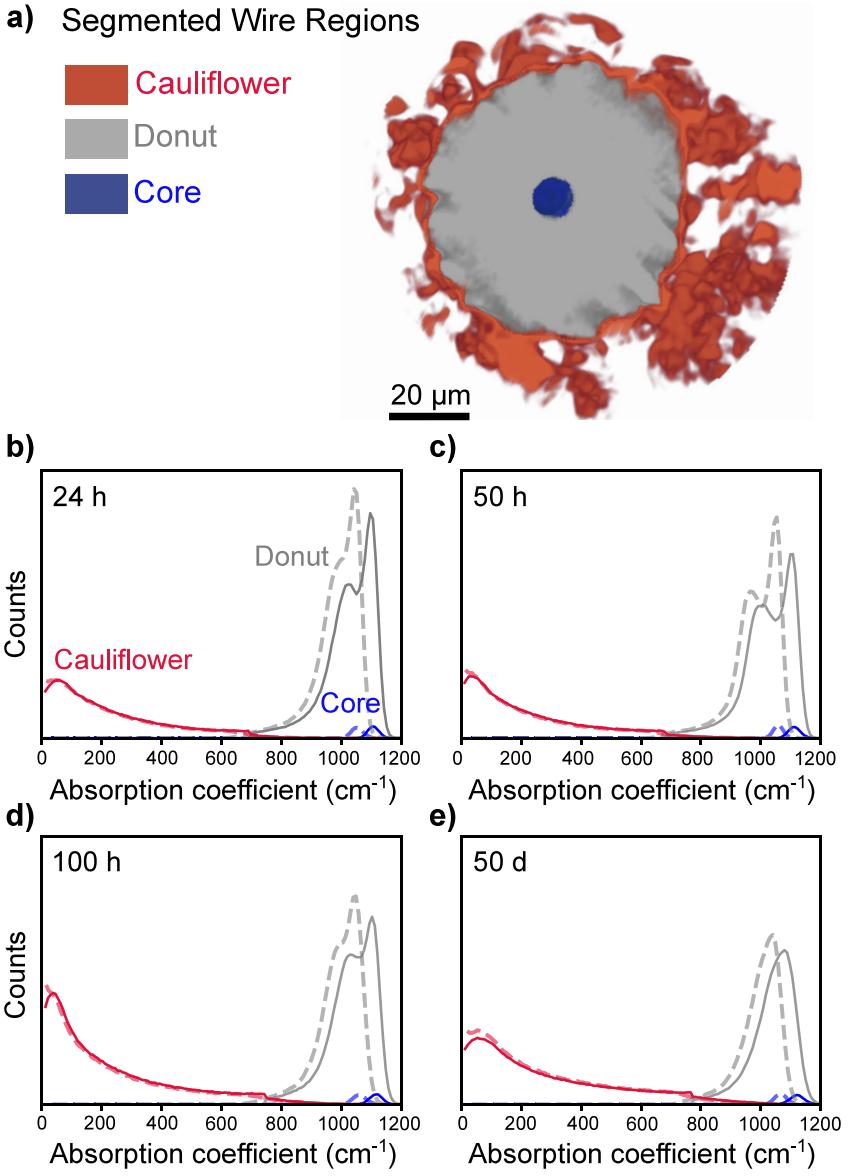

Figure 4. (a) Segmentation of Pt/Rh wires into three ROIs − "core" (blue), "donut" (gray), and "cauliflower" (red) for image analysis. (b) Stack histograms of μ from each ROI, showing the extent of degradation and material loss from each catalyst wire with time on stream (solid line: 23.300 keV, dotted line: 23.208 keV) after (b) 24 h, (c) 50 h, (d) 100 h, and (e) 50 days. A plot of stack histograms with y-axis in a logarithmic scale has been shown in SI Figure S12. The decrease in μ values at 23.208 keV, observed as a response to change in measurement energy, indicates a selective response to Rh content in the ROI.

distribution in the protrusion,[4,13] here, we could study quantitative 3D spatially resolved element distribution in the entire wire in a high-throughput and noninvasive manner.

The individual Rh and Pt density distributions in each ROI were therefore analyzed as violin plots to study changes in local elemental composition as a function of reaction time (Figure 5a−d and SI section 4.1−4.2). For both Pt and Rh, the core ROI for each catalyst showed constant density across all slices and was independent of time on stream (Figure 5a,c and SI Figures S16 and S17). The average core ROI density of Rh and Pt for all catalysts was calculated to be 1.23 ± 0.02 and 20.36 ± 0.10 g/cm^3, respectively, corresponding to 5.69 ± 0.05 wt % Rh and 94.31 ± 0.05 wt % Pt (SI Tables S7 and S8). This reflects the starting composition of the fresh gauze catalyst and confirms the absence of any aging effects in the wire core ROI, as discussed previously (Figure 4).

The cauliflower ROI, on the other hand, showed distinct changes in both local Rh and Pt density (Figure 5b,d). The broad Rh density distribution after 100 h of reaction time shows an apparent enrichment of Rh in the cauliflower ROI with increasing time on stream (Figure 5d). Conversely, the lower Rh density after 50 days is unsurprising due to the observed breakage of entire protrusions from the central wire (Figure 2), which affects both Pt and Rh loss, as shown in Figure 4e. The significantly lower average Pt density in the cauliflower ROI (6−8 g/cm^3, Figure 5b) as compared to the core ROI (~20 g/cm^3, Figure 5a) reflects the expected Pt loss during the time on stream and correlative material loss observed already after 24 h of reaction time. The higher average Pt density after 50 days is proposed to be due to aggregation of Pt in fewer large protrusions (Figure 5b). The dramatic decrease in average Pt density (roughly ~75%) from

https://doi.org/10.1021/acs.jpcc.4c00041
J. Phys. Chem. C 2024, 128, 5053−5063

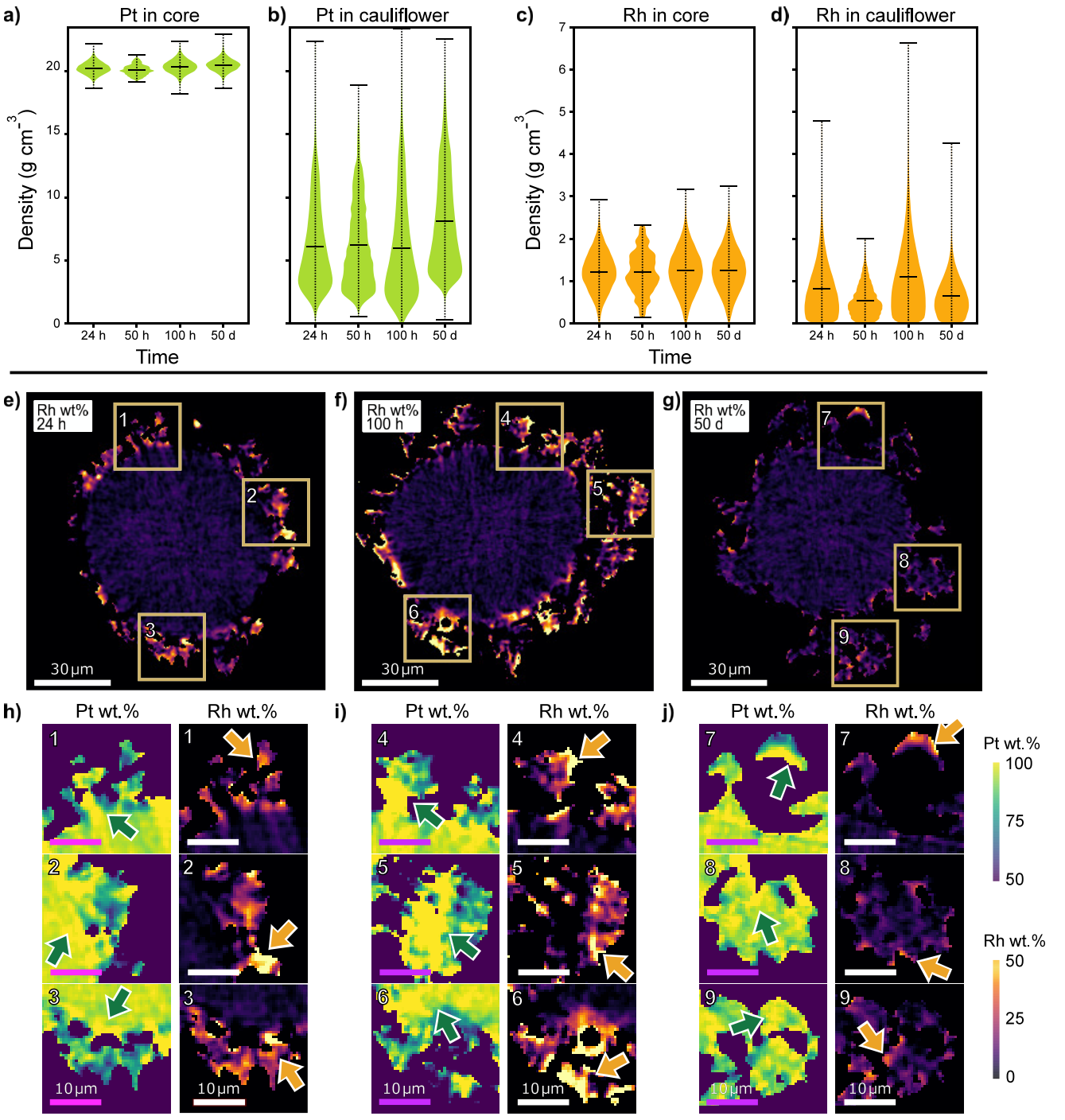

Figure 5. Violin plots based on the density distribution of the Pt/Rh gauze wires with time on stream of Pt for (a) core ROI and (b) cauliflower ROI and Rh for (c) core ROI and (d) cauliflower ROI. The central bar indicates mean density, with upper and lower brackets showing minimum and maximum density variations in the corresponding ROI. Distributions are formed from the sum of individual slices across the sample volume. Spatially resolved and thresholded Rh distribution (up to 50 wt %) in the wire cross sections for a reaction time of (e) 24 h, (f) 100 h, (g) 50 days (scale bar 30 μm), along with selected protrusions in panels (h)−(j), showing local changes in calculated Rh wt % and Pt wt % (scale bar 10 μm). Orange arrows indicate regions of high Rh wt %. Green arrows indicate regions of high Pt wt %.

the core ROI to the cauliflower ROI shows that despite the presence of Rh as a structural stabilizer, a substantial amount of Pt is still lost from the wire exterior, highlighting the persistent problem with this industrial catalyst system. A comparatively smaller decrease in average Rh density (Figure 5c,d) from ∼1.2 g/cm^3 in the core ROI to 0.6−1.1 g/cm^3 in the cauliflower ROI indicates enrichment of Rh within the protrusions, probably coupled to Pt loss. The wire aged for 50 h is considered as an anomalous sample, showing generally lower Pt and Rh densities due to the selection of a wire from close to an intersection point, resulting in a general absence of protrusions on one side of the surface (Figure 2c, SI Figures S1−S5).

A larger standard deviation and nonsymmetric violin plot distributions were observed for the cauliflower ROI in all samples (Figure 5b−d), indicating greater variation in Pt and

https://doi.org/10.1021/acs.jpcc.4c00041
J. Phys. Chem. C 2024, 128, 5053−5063

Rh within the protrusions, mainly due to metal segregation within these porous structures. Notably, this information cannot be derived quantitatively from single energy STXM-CT data but requires an element-sensitive approach, as outlined here. Although discrete regions containing isolated Pt were observed in all samples, the segregation of Pt and Rh is not necessarily mutually exclusive, as shown by overlapping Rh regions (SI section 4.3). Literature studies have reportedly confirmed Rh segregation to occur in the form of Rh_2O_3 or surface metal aggregates.[7,17] It is important to note that Rh enrichment is not necessarily limited to a surface phenomenon, but also occurs in the deeper layers of the catalysts such as the outer regions of the donut ROI. Additionally, studying large wire regions revealed element distribution in a 3D spatially resolved manner. Using X-ray resonant STXM-CT, changes in Rh and Pt density were observed throughout the entire wires, revealing a loss in the homogeneity of the catalyst material up to several μm below the surface region.

To further understand the effects of material loss, the local Pt and Rh wt % per voxel were determined and visualized (Figure 5e−g and SI Figures S23−S26). After 24 h on stream, the Rh wt % was predominantly higher around the surface of the protrusions and voids, with enrichment of up to 50 wt % Rh in some regions. This enrichment relates to the dominant presence of metal aggregates found in the literature.[4,17] In contrast, the local Pt wt % was found to be higher in the center of individual protrusions up to 100 h. This confirms that degradation mainly follows a surface etching pathway also in technical-scale catalysts. After 100 h, protrusions generally covered larger areas (Figure 5f,i and SI video), with higher local Rh enrichment (Figure 5d). Literature studies using APT previously showed the presence of metal oxides mainly along the surface grain boundaries followed by Rh depletion beneath the oxide layer, by probing within the few nm depths of the catalyst.[17,46] The study of larger samples, such as surface protrusions, performed in the literature showed Rh distribution of varying wt % in the center region of such structures via quantitative EMP, with the center of the protrusions showing lower Rh enrichment. This could also be validated using the quantitative composition study implemented here. However, the literature EMP studies could not be applied to the porous regions within the protrusions for a quantitative analysis. A qualitative and bulk-averaged XRD study was therefore used to confirm the Rh enrichment on the outer regions of the protrusions.[4] In comparison to our results, the XRD analysis seems to underestimate the Rh enrichment around the surface of hollow pores. In these regions, quantitative resonant STXM-CT reveals relatively higher Rh wt %. This shows that the lack of appropriate quantitative depth analysis within these PGM catalysts hinders the observation of holistic changes experienced in catalyst properties and behavior under reaction conditions. Notably, prolonged industrial operation for up to 50 days showed a relative decrease in Rh wt % and higher Pt wt % in the cauliflower ROI compared to the other samples (excluding the anomalous sample extracted from the gauze aged for 50 h). This is significant as the main degradation mechanism in the literature has mainly been proposed as Pt loss. This could indicate a threshold for Pt depletion beyond which the relative loss of Pt decelerates, whereas Rh continues to react. This continued active participation of Rh may be one underlying cause of the change in reaction selectivity toward N_2 after prolonged industrial use.[12] Other possibilities include breakage of complete protrusions from the wire and redistribution of Pt at an advanced aging time, therefore resulting in more heterogeneous Pt distribution after 50 days (Figure 5b). Interestingly, the newly exposed surface of the donut ROI after 50 days does not appear to undergo corrosion, although the reason for this remains unclear.

A broader sample screening at further reaction times by resonant STXM-CT may clarify the long-term material loss mechanism in future studies. Previous studies performed using EMP and XRD suggested an eventual equiatomic surface composition of Pt and Rh responsible for the catalyst restructuring. However, the Pt/40% Rh wire had not necessarily shown reduced restructuring in order to attain this equiatomic composition.[4] Here, we could show that the percentage distribution of elements spatially varies within the wire as a function of reaction time. This indicates that the resonant STXM-CT gives access to information beyond surface composition studies, now extended to 3D space in a quantitative manner, covering the entire wire surface, subsurface, and bulk. This high-throughput approach is considerably more representative of the parent technical catalyst samples than current literature approaches. The visualization of material loss, which is thought to occur from the development of hot spots on the surfaces, resulting in such material segregation was observed here as a function of reaction time. Such results may further be exploited to improve the accuracy of simulation studies to understand the effect of local temperature gradients on the elemental distribution, which are primarily done based on fresh or model Pt/Rh gauzes, thereby mainly ignoring the effects of aging on both the gauze geometry and the local chemical composition.[47]

4. CONCLUSIONS

Degradation of PGM gauze catalysts is a persistent problem in industrial heterogeneous catalysis, which is aggravated by the difficulty in studying technical catalyst systems based entirely on (noble) metals. Here, resonant STXM-CT provided quantitative 3D morphological information and chemical distribution of technical Pt/Rh gauze catalysts with ∼2 μm spatial resolution in a noninvasive manner. This quantitative method revealed changes in local Pt and Rh content within entire 76 μm × 29 μm (horizontal × vertical) wire samples after 24 h to 50 days under NH_3 oxidation conditions. While different reaction mechanisms have been proposed in the literature, resonant STXM-CT exhibited a material loss progressing from the surface to the inner regions of the catalyst. Since the wire core did not show any changes in composition even after 50 days on stream, there was no indication of volume diffusion from the core ROI to the exterior donut ROI to compensate for material loss during protrusion formation. The significant Pt loss, later accompanied by relatively low Rh loss, was therefore deconvoluted within individual protrusions as a function of time on stream. The broad length scale covered designates this as a high-throughput and 3D spatially resolved investigation of Pt/Rh gauze degradation. It should be noted that in comparison to the available literature, full-field X-ray absorption-contrast imaging would be difficult around the Rh K-edge due to pure PGM content in the samples and the limited dynamic range of area detectors. Using a single-photon counting pixel detector with the transmitted beam being spread across many pixels without dark counts resulted in an effective dynamic range, essential for quantitative measurement of highly-absorbing samples, which is not achievable using other detectors.The

https://doi.org/10.1021/acs.jpcc.4c00041
J. Phys. Chem. C 2024, 128, 5053−5063

characterization approach shown here is technically straightforward at typical synchrotron microprobe beamlines. It offers renewed opportunities to further characterize the degradation of technical PGM gauze catalysts and explore the effects of reaction conditions, gauze geometry, and catalyst composition, for example. Element-specific chemical composition of such challenging industrial samples was made possible exclusively with synchrotron-based STXM-CT, yielding technically representative results on extended sample volumes. Future efforts are required to stabilize such PGM gauze catalysts to increase process efficiency and sustainability. Further determination of chemical species and possible degradation mechanisms may also be possible with spatially resolved *in situ* or *operando* spectrotomography under reaction conditions.[48−50] However, the harsh conditions of NH_3 oxidation present a technical challenge. This research hereby establishes a framework for a high-resolution and high-throughput study of PGM catalysts and similar systems. The future aim is to exploit such characterization data to rationalize and identify the most stable and sustainable industrial catalysts for NH_3 oxidation and related reaction systems.

■ ASSOCIATED CONTENT

Data Availability Statement

The STXM-CT data was acquired at the P06 beamline of PETRA III (Deutsches-Elektronen Synchrotron DESY, Hamburg). The final processed and cropped 3D volumes for two measurement energies above and below the Rh K-edge for each gauze wire after their respective reaction times have been stored as stack of slices of the tomographic data sets in KITopen, the central repository of the Karlsruhe Institute of Technology. The following are the DOIs of the respective data sets: 10.35097/1932, 50 days aged wire; 10.35097/1931, 100 h aged wire; 10.35097/1930, 50 h aged wire; 10.35097/1929, 24 h aged wire.

Supporting Information

The Supporting Information is available free of charge at https://pubs.acs.org/doi/10.1021/acs.jpcc.4c00041.

Additional electron microscopy images of all catalysts, detailed step-by-step procedure for tomographic data reconstruction and image processing, calculation procedure for physical measurements including diameter and surface area, calculation procedure for chemical measurements including local catalyst composition, further information on statistical analysis; video demonstrating the cross-sectional view of a sample aged for 100 h of reaction time (PDF)

Video demonstrating the cross-sectional view of a sample aged for 100 h of reaction time (MP4)

■ AUTHOR INFORMATION

Corresponding Author

Thomas L. Sheppard − *Institute for Chemical Technology and Polymer Chemistry, Karlsruhe Institute of Technology, 76131 Karlsruhe, Germany; Institute of Catalysis Research and Technology, Karlsruhe Institute of Technology, 76344 Eggenstein-Leopoldshafen, Germany;* Present Address: Institute of Chemical Technology, Leipzig University, Linnéstrasse 3, 04103 Leipzig, Germany.; orcid.org/0000-0002-8891-985X; Email: thomas.sheppard@kit.edu

Authors

Srashtasrita Das − *Institute for Chemical Technology and Polymer Chemistry, Karlsruhe Institute of Technology, 76131 Karlsruhe, Germany; Institute of Catalysis Research and Technology, Karlsruhe Institute of Technology, 76344 Eggenstein-Leopoldshafen, Germany;* orcid.org/0000-0002-5025-1663

Michael E. Stuckelberger − *Center for X-ray and Nano Science CXNS, Deutsches Elektronen-Synchrotron DESY, 22607 Hamburg, Germany*

Jan Pottbacker − *Institute of Chemical Reaction Engineering, Hamburg University of Technology, 21073 Hamburg, Germany;* Present Address: BASF SE, 67063 Ludwigshafen, Germany

Sven Jakobtorweihen − *Institute of Chemical Reaction Engineering, Hamburg University of Technology, 21073 Hamburg, Germany; Reacnostics Modelling & Data Science GmbH, 20457 Hamburg, Germany;* orcid.org/0000-0001-5492-8304

Christian G. Schroer − *Center for X-ray and Nano Science CXNS, Deutsches Elektronen-Synchrotron DESY, 22607 Hamburg, Germany; Department Physik, Universität Hamburg, 22761 Hamburg, Germany; Helmholtz Imaging, Deutsches Elektronen-Synchrotron DESY, 22607 Hamburg, Germany;* orcid.org/0000-0002-9759-1200

Raimund Horn − *Institute of Chemical Reaction Engineering, Hamburg University of Technology, 21073 Hamburg, Germany; Reacnostics GmbH, 20457 Hamburg, Germany*

Complete contact information is available at: https://pubs.acs.org/10.1021/acs.jpcc.4c00041

Author Contributions

S.D., C.G.S, R.H., and T.L.S. conceived and designed the study. S.D., M.E.S., C.G.S., and T.L.S. developed the experimental methods. S.D. and T.L.S. developed the code to analyze the data. S.D., M.E.S., C.G.S., and T.L.S. verified the data. S.D., M.E.S., and T.L.S. performed the experiments. J.P., S.J., and R.H. provided the materials. S.D. and T.L.S. wrote the original draft. All authors contributed to the revision of the manuscript. C.G.S., R.H., and T.L.S. supervised the work. R.H. and T.L.S. were responsible for acquisition of funding.

Notes

The authors declare no competing financial interest.

■ ACKNOWLEDGMENTS

This work was funded by the German Federal Ministry of Education and Research (Bundesministerium für Bildung und Forschung, BMBF), project COSMIC − 05K19VK4. The authors acknowledge PETRA III, DESY (Hamburg, Germany), a member of the Helmholtz Association, for provision of the beamtime with proposal ID I-20200244. The P06 group of PETRA III is kindly acknowledged for their support during the experiment setup. The authors would like to thank Yara International ASA for provision of fresh and industrially aged gauzes. Satish Kulkarni, Thomas Keller (NanoLab, DESY, Hamburg), Tobias Krekeler and Lida Wang (Electron Microscopy Unit BeEM, Technical University of Hamburg) are acknowledged for their support during sample preparation and acquisition of SEM images. We kindly acknowledge Jan-Dierk Grunwaldt (Karlsruhe Institute of Technology, Karlsruhe, Germany) for discussion of results.

REFERENCES

(1) Handforth, S. L.; Tilley, J. N. Catalysts for Oxidation of Ammonia to Oxides of Nitrogen. *Ind. Eng. Chem.* **1934**, *26*, 1287−1292.

(2) Hatscher, S. T.; Fetzer, T.; Wagner, E.; Kneuper, H.-J. Ammonia Oxidation. In *Handbook of Heterogeneous Catalysis*; John Wiley & Sons, Ltd, 2008; pp 2575−2592. DOI: 10.1002/9783527610044.hetcat0130.

(3) McCabe, R. W.; Pignet, T.; Schmidt, L. D. Catalytic Etching of Platinum in NH3 Oxidation. *J. Catal.* **1974**, *32*, 114−126.

(4) Hannevold, L.; Nilsen, O.; Kjekshus, A.; Fjellvåg, H. Reconstruction of Platinum−Rhodium Catalysts during Oxidation of Ammonia. *Appl. Catal. A Gen.* **2005**, *284*, 163−176.

(5) Bergene, E.; Tronstad, O.; Holmen, A. Surface Areas of Pt−Rh Catalyst Gauzes Used for Ammonia Oxidation. *J. Catal.* **1996**, *160*, 141−147.

(6) Farrauto, R. J.; Lee, H. C. Ammonia Oxidation Catalysts with Enhanced Activity. *Ind. Eng. Chem. Res.* **1990**, *29*, 1125−1129.

(7) Fierro, J. L. G.; Palacios, J. M.; Tomas, F. Characterization of Catalyst and Catchment Gauzes Used in Medium- and Low-Pressure Ammonia Oxidation Plants. *J. Mater. Sci.* **1992**, *27*, 685−691.

(8) Bockholt, A.; Harding, I. S.; Nix, R. M. Hydrogen Cyanide Synthesis on Polycrystalline Platinum and 90:10 Platinum-Rhodium Surfaces. *J. Chem. Soc., Faraday Trans.* **1997**, *93*, 3869−3878.

(9) Kondratenko, V. A. Mechanistic Aspects of the Andrussow Process over Pt−Rh Gauzes. Pathways of Formation and Consumption of HCN. *Appl. Catal. A Gen.* **2010**, *381*, 74−82.

(10) Lim, J.; Fernández, C. A.; Lee, S. W.; Hatzell, M. C. Ammonia and Nitric Acid Demands for Fertilizer Use in 2050. *ACS Energy Lett.* **2021**, *6*, 3676−3685.

(11) Rasmussen, K. D.; Wenzel, H.; Bangs, C.; Petavratzi, E.; Liu, G. Platinum Demand and Potential Bottlenecks in the Global Green Transition: A Dynamic Material Flow Analysis. *Environ. Sci. Technol.* **2019**, *53*, 11541−11551.

(12) Pérez−Ramírez, J.; Kondratenko, E. V.; Novell-Leruth, G.; Ricart, J. M. Mechanism of Ammonia Oxidation over PGM (Pt, Pd, Rh) Wires by Temporal Analysis of Products and Density Functional Theory. *J. Catal.* **2009**, *261*, 217−223.

(13) Fjellvåg, A. S.; Jørgensen, P. S.; Waller, D.; Wragg, D. S.; Di Michiel, M.; Sjåstad, A. O. Mechanism of Grain Reconstruction of Pd and Pd/Ni Wires during Pt−Catchment. *Materialia* **2022**, *21*, No. 101359.

(14) Pura, J.; Kwaśniak, P.; Jakubowska, D.; Jaroszewicz, J.; Zdunek, J.; Garbacz, H.; Mizera, J.; Gierej, M.; Laskowski, Z. Investigation of Degradation Mechanism of Palladium−Nickel Wires during Oxidation of Ammonia. *Catal. Today* **2013**, *208*, 48−55.

(15) Nilsen, O.; Kjekshus, A.; Fjellvåg, H. Reconstruction and Loss of Platinum Catalyst during Oxidation of Ammonia. *Appl. Catal. A Gen.* **2001**, *207*, 43−54.

(16) Li, T.; Bagot, P. A. J.; Marquis, E. A.; Edman Tsang, S. C.; Smith, G. D. W. Atomic Engineering of Platinum Alloy Surfaces. *Ultramicroscopy* **2013**, *132*, 205−211.

(17) Bagot, P. A. J.; Kruska, K.; Haley, D.; Carrier, X.; Marceau, E.; Moody, M. P.; Smith, G. D. W. Oxidation and Surface Segregation Behavior of a Pt-Pd-Rh Alloy Catalyst. *J. Phys. Chem. C* **2014**, *118*, 26130−26138.

(18) Resta, A.; Hejral, U.; Blomberg, S.; Albertin, S.; Vlad, A.; Garreau, Y.; Chatelier, C.; Venturini, F.; Ferrer, P.; Held, G.; et al. Ammonia Oxidation over a Pt25Rh75(001) Model Catalyst Surface: An Operando Study. *J. Phys. Chem. C* **2020**, *124*, 22192−22199.

(19) Ivashenko, O.; Johansson, N.; Pettersen, C.; Jensen, M.; Zheng, J.; Schnadt, J.; Sjåstad, A. O. How Surface Species Drive Product Distribution during Ammonia Oxidation: An STM and Operando APXPS Study. *ACS Catal.* **2021**, *11*, 8261−8273.

(20) Kumar, S.; Waller, D.; Fjellvåg, H.; Sjåstad, A. O. Development of Custom Made Bimetallic Alloy Model Systems Based on Platinum-Rhodium for Heterogeneous Catalysis. *J. Alloys Compd.* **2019**, *786*, 1021−1029.

(21) Das, S.; Pashminehazar, R.; Sharma, S.; Weber, S.; Sheppard, T. L. New Dimensions in Catalysis Research with Hard X-Ray Tomography. *Chemie Ing. Technol.* **2022**, *94*, 1591−1610.

(22) Grunwaldt, J.-D.; Wagner, J. B.; Dunin-Borkowski, R. E. Imaging Catalysts at Work: A Hierarchical Approach from the Macro- to the Meso- and Nano-Scale. *ChemCatChem.* **2013**, *5*, 62−80.

(23) Pura, J.; Wieciński, P.; Kwaśniak, P.; Zwolińska, M.; Garbacz, H.; Zdunek, J.; Laskowski, Z.; Gierej, M. Investigation of the Degradation Mechanism of Catalytic Wires during Oxidation of Ammonia Process. *Appl. Surf. Sci.* **2016**, *388*, 670−677.

(24) Trevorah, R. M.; Chantler, C. T.; Schalken, M. J. Solving Self-Absorption in Fluorescence. *IUCrJ.* **2019**, *6*, 586−602.

(25) Gao, Z.; Odstrcil, M.; Böcklein, S.; Palagin, D.; Holler, M.; Sanchez, D. F.; Krumeich, F.; Menzel, A.; Stampanoni, M.; Mestl, G.; et al. Sparse Ab Initio X-Ray Transmission Spectrotomography for Nanoscopic Compositional Analysis of Functional Materials. *Sci. Adv.* **2021**, *7*, No. eabf6971.

(26) Ihli, J.; Ferreira Sanchez, D.; Jacob, R. R.; Cuartero, V.; Mathon, O.; Krumeich, F.; Borca, C.; Huthwelker, T.; Cheng, W. C.; Shu, Y. Y.; et al. Localization and Speciation of Iron Impurities within a Fluid Catalytic Cracking Catalyst. *Angew. Chemie - Int. Ed.* **2017**, *56*, 14031−14035.

(27) Johansson, G. A.; Tyliszczak, T.; Mitchell, G. E.; Keefe, M. H.; Hitchcock, A. P. Three-Dimensional Chemical Mapping by Scanning Transmission X-Ray Spectromicroscopy. *J. Synchrotron Radiat.* **2007**, *14*, 395−402.

(28) Meirer, F.; Kalirai, S.; Morris, D.; Soparawalla, S.; Liu, Y.; Mesu, G.; Andrews, J. C.; Weckhuysen, B. M. Life and Death of a Single Catalytic Cracking Particle. *Sci. Adv.* **2015**, *1*, No. e1400199.

(29) Meirer, F.; Morris, D. T.; Kalirai, S.; Liu, Y.; Andrews, J. C.; Weckhuysen, B. M. Mapping Metals Incorporation of a Whole Single Catalyst Particle Using Element Specific X-Ray Nanotomography. *J. Am. Chem. Soc.* **2015**, *137*, 102−105.

(30) Cova, S. D.; Ghioni, M. Single-Photon Counting Detectors. *IEEE Photonics J.* **2011**, *3*, 274−277.

(31) Pottbacker, J.; Jakobtorweihen, S.; Behnecke, A. S.; Abdullah, A.; Özdemir, M.; Warner, M.; Menon, M.; Bujalski, J. M.; Waller, D.; Korup, O.; et al. Resolving Gradients in an Ammonia Oxidation Reactor under Industrial Conditions: A Combined Experimental and Simulation Study. *Chem. Eng. J.* **2022**, *439*, No. 135350.

(32) Noei, H.; Vonk, V.; Keller, T. F.; Roehlsberger, R.; Stierle, A. DESY NanoLab. *J. large-scale Res. Facil.* **2016**, *2*, A76.

(33) Falkenberg, G.; Seiboth, F.; Koch, F.; Falch, K. V.; Schropp, A.; Brückner, D.; Garrevoet, J. CRL Optics and Silicon Drift Detector for P06 Microprobe Experiments at 35 KeV. *Powder Diffr.* **2020**, *35*, S34−S37.

(34) Harris, C. R.; Millman, K. J.; van der Walt, S. J.; Gommers, R.; Virtanen, P.; Cournapeau, D.; Wieser, E.; Taylor, J.; Berg, S.; Smith, N. J.; et al. Array Programming with NumPy. *Nature* **2020**, *585*, 357−362.

(35) Hunter, J. D. Matplotlib: A 2D Graphics Environment. *Comput. Sci. Eng.* **2007**, *9*, 90−95.

(36) Virtanen, P.; Gommers, R.; Oliphant, T. E.; Haberland, M.; Reddy, T.; Cournapeau, D.; Burovski, E.; Peterson, P.; Weckesser, W.; Bright, J.; et al. SciPy 1.0: Fundamental Algorithms for Scientific Computing in Python. *Nat. Methods* **2020**, *17*, 261−272.

(37) Trampert, J.; Leveque, J.-J. Simultaneous Iterative Reconstruction Technique: Physical Interpretation Based on the Generalized Least Squares Solution. *J. Geophys. Res. Solid Earth* **1990**, *95*, 12553−12559.

(38) van Aarle, W.; Batenburg, K. J.; Palenstijn, W. J.; Cant, J.; Sijbers, J.; Janssens, E.; Dabravolski, A.; De Beenhouwer, J.; Bleichrodt, F. Fast and Flexible X-Ray Tomography Using the ASTRA Toolbox. *Opt. Express* **2016**, *24*, 25129−25147.

(39) van Aarle, W.; Palenstijn, W. J.; De Beenhouwer, J.; Altantzis, T.; Bals, S.; Batenburg, K. J.; Sijbers, J. The ASTRA Toolbox: A Platform for Advanced Algorithm Development in Electron Tomography. *Ultramicroscopy* **2015**, *157*, 35−47.

https://doi.org/10.1021/acs.jpcc.4c00041
J. Phys. Chem. C 2024, 128, 5053−5063

(40) Thevenaz, P.; Ruttimann, U. E.; Unser, M. A Pyramid Approach to Subpixel Registration Based on Intensity. *IEEE Trans. Image Process.* **1998**, *7*, 27−41.
(41) Schindelin, J.; Arganda-Carreras, I.; Frise, E.; Kaynig, V.; Longair, M.; Pietzsch, T.; Preibisch, S.; Rueden, C.; Saalfeld, S.; Schmid, B.; et al. Fiji: An Open-Source Platform for Biological-Image Analysis. *Nat. Methods* **2012**, *9*, 676−682.
(42) Ravel, B.; Newville, M. ATHENA, ARTEMIS, HEPHAESTUS: Data Analysis for X-Ray Absorption Spectroscopy Using IFEFFIT. *J. Synchrotron Radiat.* **2005**, *12*, 537−541.
(43) Hannevold, L.; Nilsen, O.; Kjekshus, A.; Fjellvåg, H. Surface Reconstruction on Noble-Metal Catalysts during Oxidation of Ammonia. *Appl. Catal. A Gen.* **2005**, *284*, 185−192.
(44) Mangipudi, K. R.; Radisch, V.; Holzer, L.; Volkert, C. A. A FIB-Nanotomography Method for Accurate 3D Reconstruction of Open Nanoporous Structures. *Ultramicroscopy* **2016**, *163*, 38−47.
(45) Weber, S.; Zimmermann, R. T.; Bremer, J.; Abel, K. L.; Poppitz, D.; Prinz, N.; Ilsemann, J.; Wendholt, S.; Yang, Q.; Pashminehazar, R.; et al. Digitization in Catalysis Research: Towards a Holistic Description of a Ni/Al2O3 Reference Catalyst for CO2Methanation. *ChemCatChem.* **2022**, *14*, No. e202101878.
(46) Li, T.; Marquis, E. A.; Bagot, P. A. J.; Tsang, S. C.; Smith, G. D. W. Characterization of Oxidation and Reduction of a Platinum−Rhodium Alloy by Atom-Probe Tomography. *Catal. Today* **2011**, *175*, 552−557.
(47) Haas, M.; Nien, T.; Fadic, A.; Mmbaga, J. P.; Klingenberger, M.; Born, D.; Etzold, B. J. M.; Hayes, R. E.; Votsmeier, M. N2O Selectivity in Industrial NH3 Oxidation on Pt Gauze Is Determined by Interaction of Local Flow and Surface Chemistry: A Simulation Study Using Mechanistic Kinetics. *Chem. Eng. Sci.* **2022**, *260*, No. 117832.
(48) Price, S. W. T.; Martin, D. J.; Parsons, A. D.; Sławiński, W. A.; Vamvakeros, A.; Keylock, S. J.; Beale, A. M.; Mosselmans, J. F. W. Chemical Imaging of Fischer−Tropsch Catalysts under Operating Conditions. *Sci. Adv.* **2017**, *3*, No. e1602838.
(49) van Ravenhorst, I. K.; Vogt, C.; Oosterbeek, H.; Bossers, K. W.; Moya-Cancino, J. G.; van Bavel, A. P.; van der Eerden, A. M. J.; Vine, D.; de Groot, F. M. F.; Meirer, F.; et al. Capturing the Genesis of an Active Fischer−Tropsch Synthesis Catalyst with Operando X-Ray Nanospectroscopy. *Angew. Chemie. Int. Ed.* **2018**, *57*, 11957−11962.
(50) Becher, J.; Sanchez, D. F.; Doronkin, D. E.; Zengel, D.; Meira, D. M.; Pascarelli, S.; Grunwaldt, J.-D.; Sheppard, T. L. Chemical Gradients in Automotive Cu-SSZ-13 Catalysts for NOx Removal Revealed by Operando X-Ray Spectrotomography. *Nat. Catal.* **2021**, *4*, 46−53.

https://doi.org/10.1021/acs.jpcc.4c00041
J. Phys. Chem. C 2024, 128, 5053−5063